Journal of Alloys and Compounds 771 (2019) 686–698

Contents lists available at ScienceDirect

Journal of Alloys and Compounds

journal homepage: http://www.elsevier.com/locate/jalcom

Influence of different organic fuels on the phase composition, structure parameters and magnetic properties of hexaferrites $BaFe_{12}O_{19}$ synthesized by the sol-gel combustion

V.A. Zhuravlev [a, *], V.I. Itin [b], R.V. Minin [b], Yu. M. Lopushnyak [a], V.A. Svetlichnyi [a], I.N. Lapin [a], D.A. Velikanov [c], I. Yu Lilenko [a]

[a] Tomsk State University, Tomsk, 634050, Russia
[b] Tomsk Scientific Center, SB RAS, Tomsk, 634021, Russia
[c] Kirensky Institute of Physics, Federal Research Center KSC SB RAS, Krasnoyarsk, 660036, Russia

ARTICLE INFO

Article history:
Received 14 February 2018
Received in revised form
12 July 2018
Accepted 29 August 2018
Available online 31 August 2018

Keywords:
Sol-gel combustion
Nanocrystalline hexaferrites
Magnetization curve
Ferromagnetic resonance
Magnetocrystalline anisotropy

ABSTRACT

Phase composition, structure parameters, morphology and basic magnetic characteristics – the specific saturation magnetization values and the magnetic anisotropy fields of the nanostructured $BaFe_{12}O_{19}$ powders prepared by the sol-gel combustion with the following annealing at 850°C for six hours are investigated. As organic fuels the following materials are used: carbamide (CON_2H_4), sucrose ($C_{12}H_{22}O_{11}$), glycine ($C_2H_5NO_2$) and citric acid ($C_6H_8O_7$). The influences of the type of the organic fuels on the properties of synthesized materials are analysed. It is shown that in the powders obtained the distribution of particles on the size, the values of saturation magnetizations and the anisotropy fields depend on the fuel type. The sample synthesized using carbamide has the smallest content of the target phase $BaFe_{12}O_{19}$, the widest particle size distribution and the lowest value of the saturation magnetization in comparison with the other samples. The narrowest distribution of the particles on the size and the highest value of the specific saturation magnetization are observed in the material synthesized with the use of citric acid as an organic fuel. A comparison of the experimental hysteresis loops with the calculated magnetization curves is made. It is shown that the paraprocess plays a significant role in the magnetization processes of the synthesized materials ($\chi_{para.} \approx 0.125*10^{-3}$ cm^3/g). A technique for determining the values of the anisotropy fields and the magnetomechanical ratios from experiments on FMR is also described. Calculations of the magnetization curve and the ferromagnetic resonance line of hexaferrites powders with uniaxial anisotropy were carried out in the independent grains approach.

1. Introduction

Hexagonal ferrites, in particular Barium hexaferrite $BaFe_{12}O_{19}$ with the crystallographic M-type structure, are broadly used to manufacture permanent magnets as well as various components for radar absorption material and microwave devices [1–5]. A vivid scientific and practical interest to this material is caused by the fact that it possesses high values of the Curie temperature (T_C), the coercive force (H_C), the saturation magnetization (σ_S) and the magnetocrystalline anisotropy field (H_{a1}). In addition, its magnetic properties are stable in a wide range of temperatures.

The manufacturing of hexaferrites is based on a traditional multioperation ceramics technology which includes a prolonged sintering of components at a high temperature. This technology is used in the world practice for many decades. The trends of its development are connected with optimizing the ways to change the composition and methods of processing the charge [6,7].

In the last decades new resources-economy ways to obtain hexaferrites are developed. They are based on the self-propagating high-temperature synthesis (SHS), which proceeds in the filtration combustion mode of a mixture of iron powders and the oxides of other elements in the atmosphere of reacting gases: oxygen or air [8–15].

One of the well-known ways to obtain the M-type Barium hexaferrite nanocrystalline powders of a homogeneous composition which is based on the SHS-processes is the sol-gel combustion

* Corresponding author. 17/62, A. Belentsa Str., Tomsk, 634050, Russia.
E-mail address: ptica@mail.tsu.ru (V.A. Zhuravlev).

https://doi.org/10.1016/j.jallcom.2018.08.294
0925-8388/

method (the burning of solutions). The main principle is to create an initial colloidal system which has the ability to react while being combusted [16–30].

Apparently, the nanocrystalline $BaFe_{12}O_{19}$ powders with M-structure (Ba-M) were first synthesized using the sol-gel combustion method in Refs. [16,17]. As an organic fuel the tetraformal trisazine (TFTA, $C_4H_{12}N_6$) or oxalic acid dihydrazide (ODH, $C_2H_6N_4O_2$) [16] and the citric acid [17] were used while metal nitrates were used as oxidants. The gel combustion product consisted of a mixture of different phases: γ-Fe_2O_3, α-Fe_2O_3 and $BaCO_3$. During the first stage the calcinations at optimal temperatures lead to the Barium monoferrite ($BaFe_2O_4$) synthesis and the emission of the coaly gases and to the formation of Ba-M hexaferrite during the second stage. It is determined that the molar ratios (citric acid/nitrate and Fe/Ba) influence the combustion process as well as the average size of crystallites significantly. As a result the nanocrystalline powders of $BaFe_{12}O_{19}$ hexaferrite with the grain sizes from 80 to 120 nm, the saturation magnetization of 59.36 emu/g and the $H_C = 5.54$ kOe are obtained [17]. It is necessary to note that the inference about the two-stage synthesis is also approved in a range of the other articles. However, as the authors of the article [18] reckon, one can realize the one-stage synthesis of Ba-M hexaferrite with the minimal amount of impurity phases.

The influence of the molar ratios Fe/Ba and citric acid/nitrate on the phase composition, the formation temperature and the $BaFe_{12}O_{19}$ crystallite sizes is analysed in the series of articles by A. Mali and A. Ataie [19–21]. The results derived in Ref. [17] were confirmed. The structure formation was studied. It was established that increasing the calcinations temperature from 1000 to 1100 °C leads to a significant enlargement of the hexaferrite grain size from 0.4 to 2.5 μm.

The article [22] is also dedicated to the solution of this problem. The article describes the process of the Ba-M powders synthesis. The influence of the molar ratios (citric acid/nitrate) with the proportions of 1:1, 1:2 and 1:3 on the powder size, morphology and magnetic properties is studied. If the proportion is 1:2 the powder obtained has the biggest magnetic moment value - of 55 emu/g. It also has a high coercive force (5000 Oe) and the maximal magnetic energy $(BH)_{max}$ is equal to $1.013 \cdot 10^6$ Gs*Oe.

The pH influence on the structure parameters and the magnetic properties of Ba-M is determined in Ref. [23]. With the pH increase the lattice parameters decrease and the X-ray density grows. The crystallites diminish in size and are less than 100 nm. The pH value also influences the phase composition of the final product. So, it's necessary to regulate it in order to synthesize the Ba-M hexaferrite free from any impurity phases. The homogeneity of the metal-citrate complexes formed in the gel depends on the pH of original solutions as well as the molar ratio of citric acid to the metal ions. This in its turn affects the regularities of combustion and the phase composition of combustion products [24].

It should be noted that most of the studies carried out provide data on the magnetic characteristics of Ba-M hexaferrite powders obtained only from the study of magnetization curves and hysteresis loops. These data are: the values of specific saturation magnetization (σ_S), residual magnetization (σ_r) and coercive force (H_c). It's known that the H_c value is proportional to the effective anisotropy field (H_{a1}). But there are no direct methods to measure the H_{a1} values of the powders and the polycrystalline hexaferrites. The knowledge of this parameter, however, is important for the practical application of hexaferrites.

There are three methods which are used to determine the value of H_{a1} via an experiment on the macroscopically isotropic polycrystalline hexaferrite powders:

- the law of approach to saturation (LAS) [31–33];
- the singular point detection (SPD) [34,35];
- the ferromagnetic resonance (FMR) method.

To satisfy the LAS applicability condition, the values of magnetizing fields (H_0) more than the values of the anisotropy field $H_0 > H_{a1}$ are needed. According to [33] the errors of the H_{a1} value estimation can be significant.

The second method is also based on the magnetization curves investigation. In the article [34] it is shown that for the uniaxial magnets with the positive constant of anisotropy the second derivative of the magnetization curve has a singularity at the value of the magnetizing field equal to the magnetocrystalline anisotropy field ($H_0 = H_{a1}$). The measurements of H_{a1} by this method are usually carried out in the pulsed magnetic fields [35].

The FMR method is a sensitive and mature technique, yielding accurate measures of the magnetocrystalline anisotropy fields and the values of the effective magnetomechanical ratio $\gamma = ge/2mc$. Here g is the effective g-factor of the material under study, e is the electron charge, m is the electron mass, and c is the speed of light. Due to this reason it is more preferable to estimate the H_{a1} of materials with the high anisotropy field values such as Ba-M hexaferrites.

In the articles [22,26,36] the results of the FMR test of the nanosized Ba-M particles at X-band frequency range are presented. These frequencies are significantly lower than the natural FMR (NFMR) frequency of the Ba-M hexaferrite $f_{NFMR} \approx (44–47)$ GHz. Due to this reason it is difficult to obtain some reliable estimations of H_{a1} and γ in this frequency range. Besides, the estimations of FMR parameters at one frequency or in a narrow frequency range give bigger errors in the assessing the values of an effective magnetomechanical ratio of the sample tested.

The FMR in the nanostructured samples of Ba-M and $Sr(Co_xTi_x)Fe_{12-2x}O_{19}$ ($0.0 \le x \le 1.0$) hexaferrites was tested at the frequencies of the EHF range (37–53) GHz in the articles [25] and [37] respectively. The analysis of resonance curve forms in this frequency range made it possible to define the values of the anisotropy fields as well as the magneto-mechanical ratios of these materials. It is to be noted that in Ref. [37] it is shown that an interpretation of the ferromagnetic resonance (FMR) spectra for hexaferrites $Sr(Co_xTi_x)Fe_{12-2x}O_{19}$ requires that the anisotropy of the magnetomechanical ratio should be taken into account in addition to the magnetocrystalline anisotropy.

It is mentioned above that during the Ba-M hexaferrite synthesis the citric acid is commonly used as a fuel. There is a series of articles [27–30] in which other organic compounds are used as a fuel. These are: aspartic acid [27], polyvinyl alcohol [28], glucose [29] and glycine [30]. In all the cases $BaFe_{12}O_{19}$ powders are synthesized. The problem of choosing the optimal fuel was not discussed. It is the article [27] where the influence of citric and aspartic acids on the structural parameters and the magnetic properties of $BaFe_{12}O_{19}$ hexaferrite is studied and the comparison of the results obtained is given. It is determined that the use of the aspartic acid instead of citric one leads to the formation of one-phase M-type hexaferrite as well as to the change of structural parameters, in particular to the increase of the average crystallite size.

Of great interest is the paper [38], in which the effect of the fuel type on the formation temperature, structural and magnetic characteristics of strontium hexaferrite $SrFe_{12}O_{19}$ (Sr-M) has been studied. In this article the citric acid, the tartaric acid, the sucrose and lactic acid were used as fuels. The synthesis scheme corresponds to the sol-gel combustion, but is somewhat complicated if compared with other studies.

The optimal temperature to form strontium hexaferrite (SrM) is 800 °C if citric or tartaric acids are used as fuels. This result was confirmed in Ref. [39], where it was shown that the calcinations at

this temperature improve the structure and enhance the magnetic properties of Sr-M hexaferrite synthesized using tartaric acid. The application of citric acid leads to the production of Sr-M with a maximum value of saturation magnetization, and the use of sucrose led to the maximum value of the coercive force [38]. The lowest magnetic characteristics are obtained when using lactic acid as a fuel.

To choose the optimal fuel it is of great interest to compare the characteristics of products synthesized by the sol-gel combustion method alongside with the use of different fuels. Thus, the current survey gives the details of synthesizing the $BaFe_{12}O_{19}$ hexaferrite powders by combustion of solutions with the use of different fuels: carbamide (CON_2H_4), sucrose ($C_{12}H_{22}O_{11}$), glycine ($C_2H_5NO_2$) and citric acid ($C_6H_8O_7$). Phase composition, structure parameters, morphology and basic magnetic characteristics of the final products are investigated. The estimations of the effective anisotropy fields and the magnetomechanical ratios of the synthesized products are made via FMR method [25,37].

2. Materials preparation

The synthesis of $BaFe_{12}O_{19}$ hexaferrite powders was carried out in a sol-gel combustion mode. The aqueous solutions of Barium nitrate and Iron nitrate were used as reagents. The aqueous solutions of carbamide, sucrose, glycine and citric acid were used as organic fuels.

The analytical grade reagents of Barium nitrate [$Ba(NO_3)_2$], Iron nitrate [$Fe(NO_3)_3 \cdot 9H_2O$], carbamide (CON_2H_4), sucrose ($C_{12}H_{22}O_{11}$), glycine ($C_2H_5NO_2$) and citric acid ($C_6H_8O_7$) were separately dissolved in distilled water at the concentration of 1M. After that they were mixed in accordance with the relationship:

Sample No 1 – {[$Ba(NO_3)_3$]: [$Fe(NO_3)_3 \cdot 9H_2O$]: [CON_2H_4] = {1:11.5}:2;
Sample No 2 – {[$Ba(NO_3)_3$]: [$Fe(NO_3)_3 \cdot 9H_2O$]}: [$C_{12}H_{22}O_{11}$] = {1:11.5}:2;
Sample No 3 – {[$Ba(NO_3)_3$]: [$Fe(NO_3)_3 \cdot 9H_2O$]}: [$C_2H_5NO_2$] = {1:11.5}:2;
Sample No 4 – {[$Ba(NO_3)_3$]: [$Fe(NO_3)_3 \cdot 9H_2O$]}: [$C_6H_8O_7$] = {1:11.5}:2.

The concentrated solution of ammonium hydroxide NH_4OH was gradually added dropwise with constant stirring to the mixtures till the pH ≈ 7.0 was obtained. The stirring was done with the EKROS-6120 magnet stirrer. The pH of the medium was measured with a digital portable pH-meter Checker HI98103 (HANNA Instruments). The resulting sol was evaporated at the temperatures of (90–95) °C for (3–5) hours. At the evaporation of water it turned into a viscous gel which ignited and burned afterwards. The combustion process of the gel was accompanied by the emission of a big amount of volatile impurities. Due to this the final product formation in the form of a loose powder was observed. Then the product obtained was calcined in the muffle furnace at the temperature of 850°C for 6 h to eliminate the organic impurities and to form the hexaferrite structure.

3. Research methods

The X-ray phase and the structure analysis of the samples obtained were carried out using a RIGAKU ULTIMA 4 powder diffractometer (CuK_α radiation). The phase composition and the structural parameters of the phases revealed are defined using a RIGAKU's full-function powder diffraction analysis package as well as the Powder Cell 2.4 program. The sizes of the coherent-scattering regions (CSR) are calculated with the Sherrer equation. The CSR are usually used for a rough estimation of the nanoparticle sizes.

The Raman spectra of the final product were registered with the InVia, Renishaw confocal dispersive Raman spectrometer with the Leica microscope. The excitation was carried out by means of the continuous-wave semiconductor laser with the wave length of 785 nm and the maximum power to 100 mWt. The diffraction lattice of 1200 line/mm provided the spectral resolution of 1 cm^{-1} and the microscope with the 50x lens provided the excitation locality to 2 μm^2.

The infrared spectra of the final product after combustion and further heat treatment were obtained on a FTIR spectrometer NICOLET 5700 with diffuse reflection attachment within the range (400–4000) cm^{-1}.

The particle size and the morphology of calcined powders were characterized by SEM (TESCAN, VEGA3 SBH). The distribution of particles according to the sizes was estimated on a sample group of not less than 600 particles.

The magnetization curves of powder samples obtained were investigated using the vibration magnetometer [40] with the Puzei electromagnet within the magnetizing field range ± 20 kOe. The measurements were carried out by the temperatures of 80 K and 295 K on the spherical samples with the diameter of ≈ 1.8 mm. The spheres were produced from composites based on epoxy resin with 60 mass% of the synthesized powders.

The measurement of FMR spectra in the framework of this survey was conducted using a standard waveguide "passing through" technique with an automated radio spectroscope in the frequency range of (37–53) GHz [25,37]. The powders of investigated materials were put in the thin-walled quartz tubes with the inner diameter of ≈0.7 mm and with the length of (10–12) mm. The weight of powder samples was ≈ 10 mg. The tubes were placed into the middle of the rectangular waveguide parallel to its wide wall. Due to this sample position the microwave magnetic field is directed alongside the tube axis. It provides the maximal interaction of the sample with the microwave radiation. The permanent magnetizing field was directed perpendicular to the wide wall of the waveguide.

4. Results and discussion

4.1. The results of X-ray research

Fig. 1 as well as Table 1 demonstrate the X-ray results of the sol-gel combustion products after heat treatment at 850°C for 6 h.

According to X-ray diffraction data all samples contain an impurity phases of hematite (α-Fe_2O_3) and magnetite (Fe_3O_4) together with the target phase of $BaFe_{12}O_{19}$. But all the peaks of Fe_3O_4 phase are hidden by more intense peaks of the Ba-M and hematite phases. The calculation of the percentage of magnetite phase was performed by separating the peaks by decompression method (separation of one broad peak into two more narrow ones).

It is impossible to select the magnetite phase reflexes at such a low content (~0.5%). For this reason, in Table 1 of the manuscript we did not indicate the presence of a magnetite phase with a content of less than 1% in final products.

The sample No 1 made with the use of carbamide contains the least amount of the target phase equal to ≈77%. The other samples have the amount of Ba-M phase more than 92%. The synthesized materials have almost the same values of the lattice constants *a* and *c* both for the target and the impurity phases. The obtained values

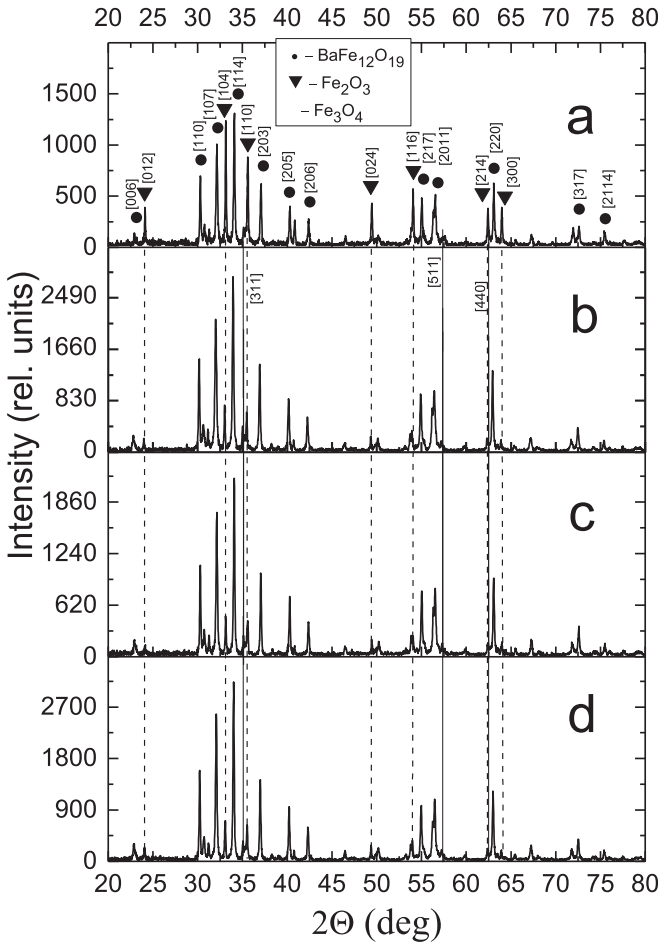

Fig. 1. XRD patterns of the samples after sol-gel combustion and heat treatment at 850°C for 6 h: No 1 – a), No 2 – b), No 3 – c), No 4 – d). X-ray reflections from Ba-M and α-Fe_2O_3 phases are labeled with different symbols. Vertical dashed lines denote the position of reflexes of the impurity phase α-Fe_2O_3. Vertical solid lines denote the location of reflexes of the impurity phase Fe_3O_4.

Table 1
XRD results of samples after sol-gel combustion and heat treatment at 850°C for 6 h.

Phase	Phase content, mass%	Lattice constant, Å		CSR, nm
		a	*c*	
Sample No 1				
$BaFe_{12}O_{19}$	76.8	5.9035	23.3130	60
α-Fe_2O_3	23.2	5.0508	13.7837	69
Sample No 2				
$BaFe_{12}O_{19}$	94.0	5.9157	23.3269	45
α-Fe_2O_3	5	5.0563	13.8061	62
Fe_3O_4	1.0	8.4667	–	30
Sample No 3				
$BaFe_{12}O_{19}$	94.1	5.9050	23.3130	61
α-Fe_2O_3	4.0	5.0478	13.7865	56
Fe_3O_4	1.9	8.3818	–	24
Sample No 4				
$BaFe_{12}O_{19}$	92.2	5.9170	23.3302	83
α-Fe_2O_3	7.8	5.1216	13.7035	24

of the lattice constants are close to the known from the literature data [1,5]. The CSR values of Ba-M phase estimated on the basis of an analysis of the physical broadening of X-ray reflexes are less than 100 nm. According to the table the CSR of the sample No 4 (synthesized with the citric acid) is more than the CSR of the products synthesized with other fuels.

4.2. Raman spectra investigation

Raman spectra of the final product are given in Fig. 2 and in Table 2. The basic articles by Kreisel et al. [41,42] were used for the interpretation. In these articles it is established that at room temperature for Ba-M structure with D_{6h} symmetry one can expect 42 active Raman modes ($11A_{1g}+14E_{1g}+17E_{2g}$) and 30 active infrared modes ($13A_{2u}+17E_{1u}$). In addition, the positions of the Raman modes of thin single-crystal films and powders almost coincide [41,42].

If to compare the Raman spectra of the products synthesized in the framework of current investigation with ones presented in the articles [41–43] it becomes clear that they are almost the same and the final product is the hexaferrite $BaFe_{12}O_{19}$. The mode at 717 cm^{-1} belongs to the tetrahedron positions of $Fe^{(3)}O_4$. The mode at 684 cm^{-1} is connected with the bipyramid $Fe^{(2)}O_5$ and the mode at 615 cm^{-1} belongs to the octahedron positions of $Fe^{(4)}O_6$, they all have the symmetry A_{1g}. The mode at 470 cm^{-1} belongs to the mixed octahedron positions of $Fe^{(1)}O_6$ and $Fe^{(5)}O_6$ with the symmetry A_{1g}, as well as the modes at 412 cm^{-1} and 337 cm^{-1}. The bands at 170 cm^{-1} and 182 cm^{-1} are the modes of a whole spinel block with the symmetry E_{1g}.

If to compare the Raman spectra of products obtained with the use of different fuels (carbamide, sucrose, glycine and citric acid) it becomes clear that the position and the intensity of the active modes are close in value (Fig. 2, Table 2).

It is to be noted that in the Raman spectra of all synthesized products one can find intensive modes at 225 cm^{-1} and 292 cm^{-1} that are absent in the Raman spectra described in Refs. [41–43]. They belong to the impurity phase α-Fe_2O_3 [44,45] which fully corresponds with the results of X-ray analysis. Modes belonging to the Fe_3O_4 phase are not observed.

The assessment of the Raman modes width on their half-height shows that this value is almost the same for all final products. Thus, the sizes of particles obtained with the use of different fuels do not differ significantly. This fact is proven by both the CSR diffraction analysis data and the SEM data given below.

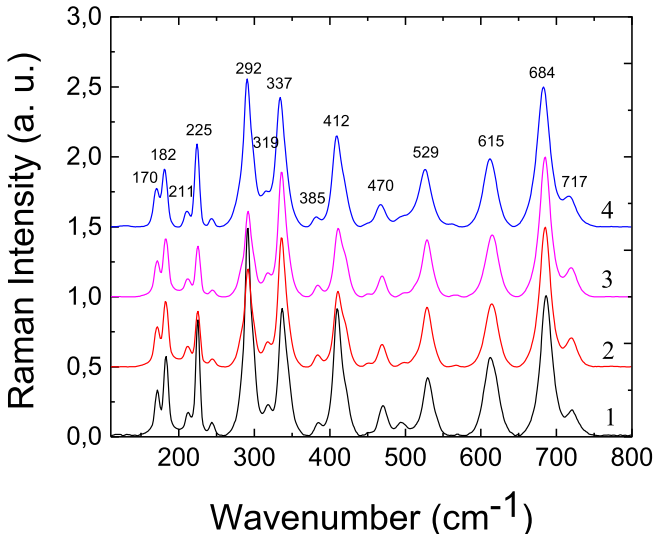

Fig. 2. Raman spectra of the final products.

Table 2
Assignment of the main Raman-active modes in Ba-M obtained by sol-gel combustion and heat treatment.

Wavenumber, cm^{-1}			Sym-metry	Assignment
[41,42]	[43]	This work, Samples Nos 1–4		
173	174	170	E_{1g}	Whole spinel block
184	186	182	E_{1g}	Whole spinel block
212	–	211	E_{1g}	
–	–	225		
250	–	245	E_{1g}	
285	–	–	E_{1g}	
–	–	292		
319	–	319	E_{2g}	
340	339	337	A_{1g}	Octahedron (mixed)
385	–	385	E_{2g}	
409	412	412	A_{1g}	$Fe^{(5)}O_6$ octahedra dominated
467	470	470	A_{1g}	Octahedra $Fe^{(1)}O_6$ and $Fe^{(5)}O_6$
529	–	529	E_{2g}	
614	618	615	A_{1g}	Octahedra $Fe^{(4)}O_6$
684	686	684	A_{1g}	Bipyramid $Fe^{(2)}O_5$
713	721	717	A_{1g}	Tetrahedra $Fe^{(3)}O_4$

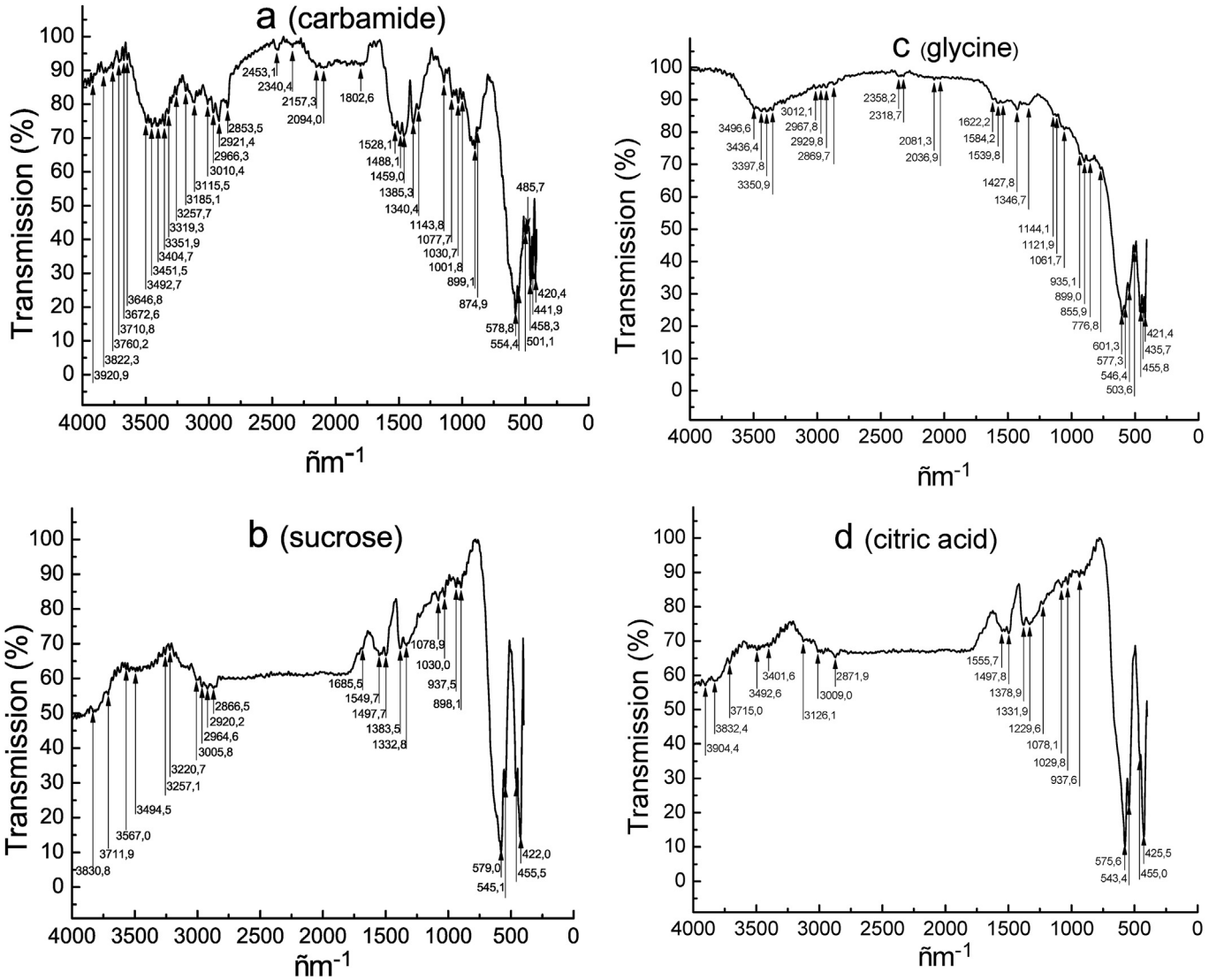

Fig. 3. IR spectra of the final products. a) – Sample No 1, b) – sample No 2, c) – sample No 3 and d) – sample No 4.

Table 3
Characteristic FTIR vibrations of $BaFe_{12}O_{19}$ obtained by sol-gel combustion and heat treatment.

IR bands, cm^{-1}				Characteristic vibrations
Samples				
No 1 (carbamide)	No 2 (sucrose)	No 3 (glycine)	No 4 (citric acid)	
3492–3351	3494	3496–3350	3492–3401	ν (O–H)
2921	2920	2930	2872	$-CH_2$
1617	–	1622	–	δ (H–O–H)
1459	1497	1427	1497	C–H
1385	1383	1346	1378	$-CH_2$
579	579	601	576	ν (Fe–O); ν (Ba–O);
554	545	548	543	ν (Fe–O); ν (Ba–O);
458	455	456	455	ν (Fe–O); ν (Ba–O);
420	422	421	425	ν (Fe–O); ν (Ba–O);

4.3. FTIR spectra

The infrared spectra of final products synthesized with the use of different fuels are shown in Fig. 3 and in Table 3. On the surface of the samples under study there is a small amount of water adsorbed after annealing. It reveals in the presence of absorption in the frequency range (3350–3500) cm^{-1} caused by the deformation vibrations of O–H groups. At 1622 cm^{-1} one can observe a weak absorption line caused by H–O–H vibrations (bending vibrations of water molecules). The bands at (1430–1500) cm^{-1} and (1350–1380) cm^{-1} are connected with the C–H and $-CH_2$ directed vibrations. A weak band at 2920 cm^{-1} can also be ascribed to the asymmetric $-CH_2$ vibrations. This fact testifies that the products obtained due to the use in the reaction of organic fuels partly remain in the final product after heat treatment and are tightly connected with its surface.

Four absorption bands in the frequency range of (600–420) cm^{-1} (Table 3) are attributed to the strong vibrations of Fe–O and Ba–O which indicate the formation of oxide hexagonal Ba-M ferromagnetic.

4.4. SEM-pictures and bar charts of particle size distribution

The SEM-pictures of sol-gel combustion products after heat treatment are shown in Fig. 4. The combustion products are mainly thin shapeless plates connected with one another. For all fuels the smallest particles have a roundish form and the size of about (100–200) nm. The biggest particles (up to 1500 nm) are the agglomerations of several particles of similar size. These particles are baked together during combustion and the subsequent heat

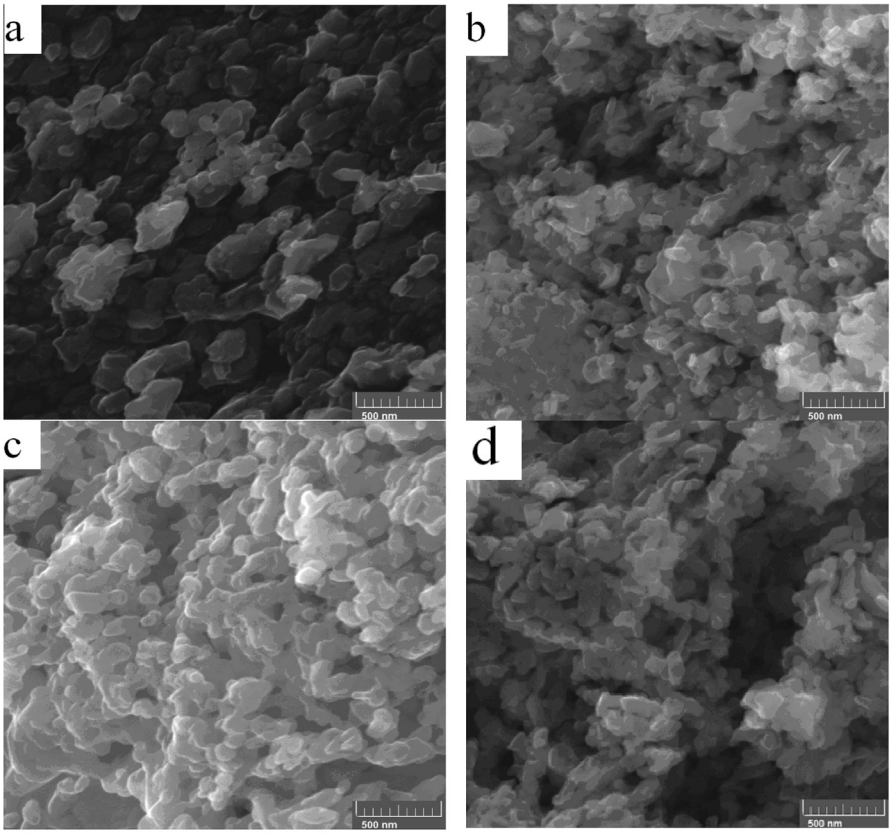

Fig. 4. SEM pictures of the final products. a) – Sample No 1, b) – sample No 2, c) – sample No 3 and d) – sample No 4.

treatment.

The bar charts of particle size distribution of the samples synthesized with different fuels are shown in Fig. 5. The comparison of bar charts demonstrates that the particles synthesized with carbamide (No 1) and glycine (No 3) have bigger sizes and a wider size distribution than the particles obtained with the use of sucrose (No 2) and citric acid (No 4).

The narrowest size distribution is typical of the product synthesized with citric acid as a fuel. The difference in particle sizes observed is primarily due to the difference in the nature of the evolution of gases that are formed and released during the combustion of selected fuels. The average particle sizes determined by the peaks on the bar charts (Fig. 5) are visibly more than the CSR sizes from Table 1.

Thus, the choice of fuel gives the opportunity to control the particle size distribution and consequently the properties of the final product.

4.5. Magnetization curve investigation

Magnetization curves of Ba-M powders are shown in Fig. 6. The measurements are carried out at two temperatures: 80 K and 295 K on the samples of spherical form with the diameter of about 1.8 mm.

The figure demonstrates that the sample No 1 with the least content of Ba-M phase and with the maximum hematite content that is a weak ferromagnetic above the Morin temperature $T_M \approx 250$ K [46] has a significantly lower specific magnetization value (σ) than the other samples. The samples No 2 and No 4 with a narrower particle size distribution (see Fig. 5) have the largest magnetization value. The hysteresis loops of these samples at 80 K and 295 K are similar, but the sample No 4 has bigger specific magnetization value.

The magnetization curves in the magnetic fields up to $H_0 = \pm$ 20 kOe do not reach saturation. It indicates the fact that the paraprocess (or a true magnetization process) significantly affects the magnetization process in the nanostructured samples obtained. The paraprocess in the nanostructured hexaferrite powders can be caused by: i) the synthesized samples contain small sized nanoparticles in the superparamagnetic state; ii) ordering of spin magnetic moments with the frustrated exchange couplings in a defective surface nanoparticles layer when the magnetizing field is applied.

The basic characteristics of the hysteresis loops are given in Table 4. In the first line the measurement temperatures are given, the numbers of the samples are in the second line. In the third line one can see the values of residual specific magnetization σ_r measured in the crossover points of dependences $\sigma(H)$ with the Y-axis at $H_0 \rightarrow \pm 0$. The value of specific saturation magnetization $\sigma_{20\ kOe}$ is measured in the maximal magnetic field $H_0 = 20$ kOe.

The ratios $\sigma_r/\sigma_{20\ kOe}$ presented in the line 5 of Table 4 are close to 0.5. According to [47] this value of the ratio $\sigma_r/\sigma_{20\ kOe}$ is typical of the processes when the chaotically oriented single-domain particles with the uniaxial anisotropy easy magnetization axis (EMA) get magnetized. Ba-M hexaferrites belong to this group [1,5]. The table testifies that the coercive force H_c grows with the increase of temperature as well. It indicates the increase of the anisotropy field value $H_{a1} = 2k_1/M_S$ in the materials under study in the temperature range from 80 K to 295 K. Here k_1 is the effective anisotropy constant; M_S is the saturation magnetization of the unit volume. In fact,

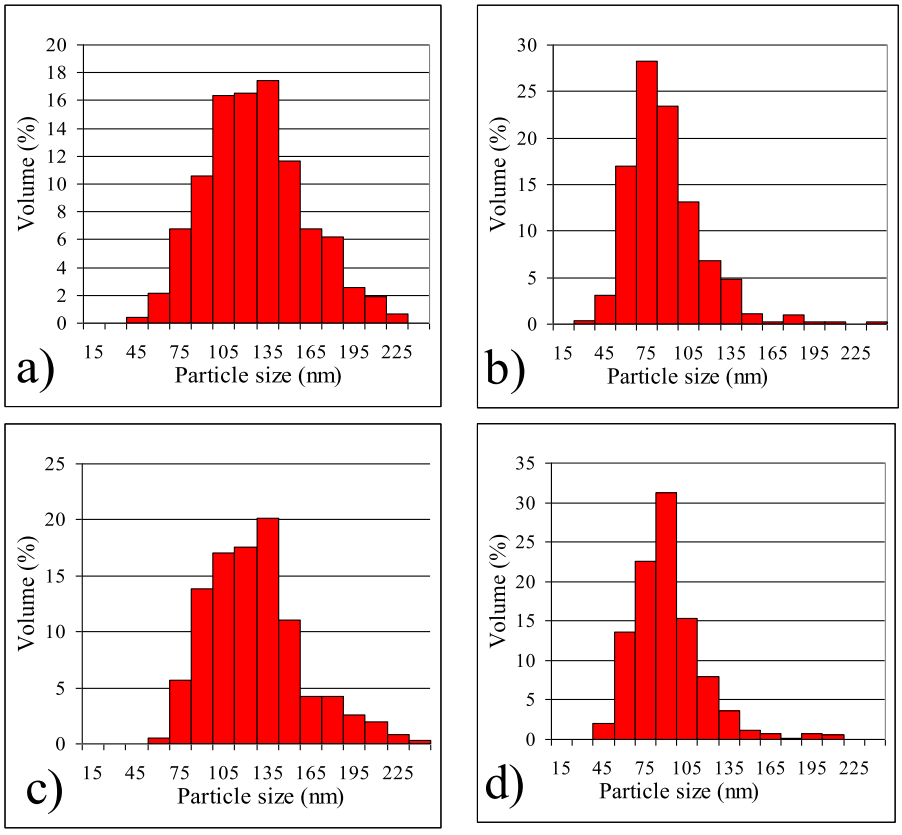

Fig. 5. Bar charts with particle size distribution of final product. a) – Sample No 1 (carbamide), b) – sample No 2 (sucrose), c) – sample No 3 (glycine) and d) – sample No 4 (citric acid).

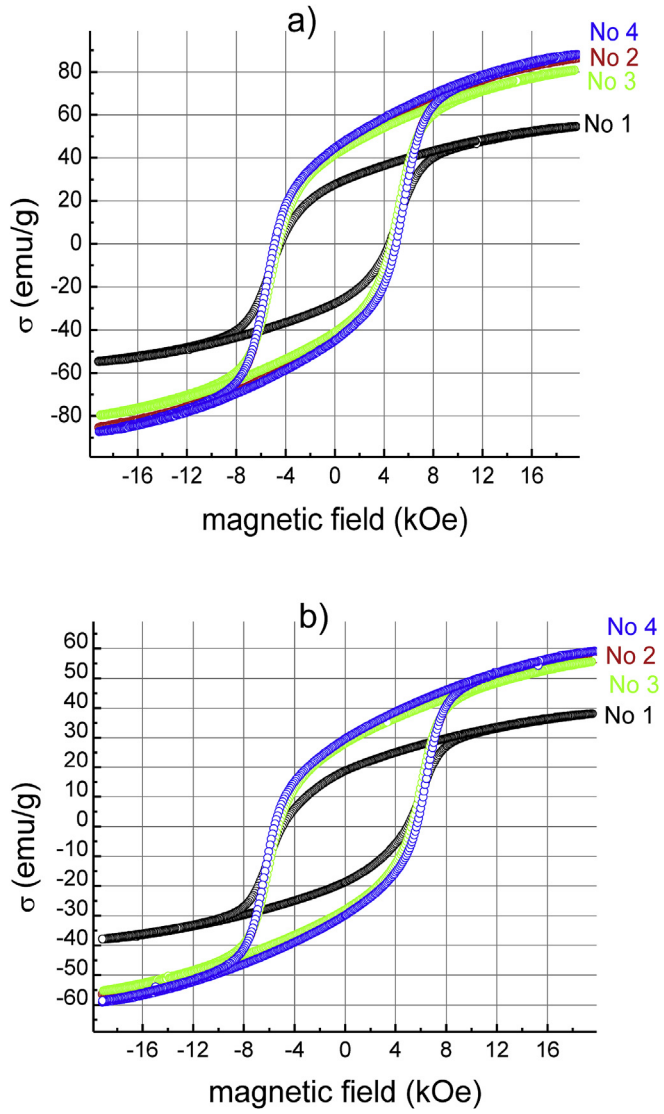

Fig. 6. Magnetization curves of the samples measured at the temperature of 80 K – a) and 295 K – b).

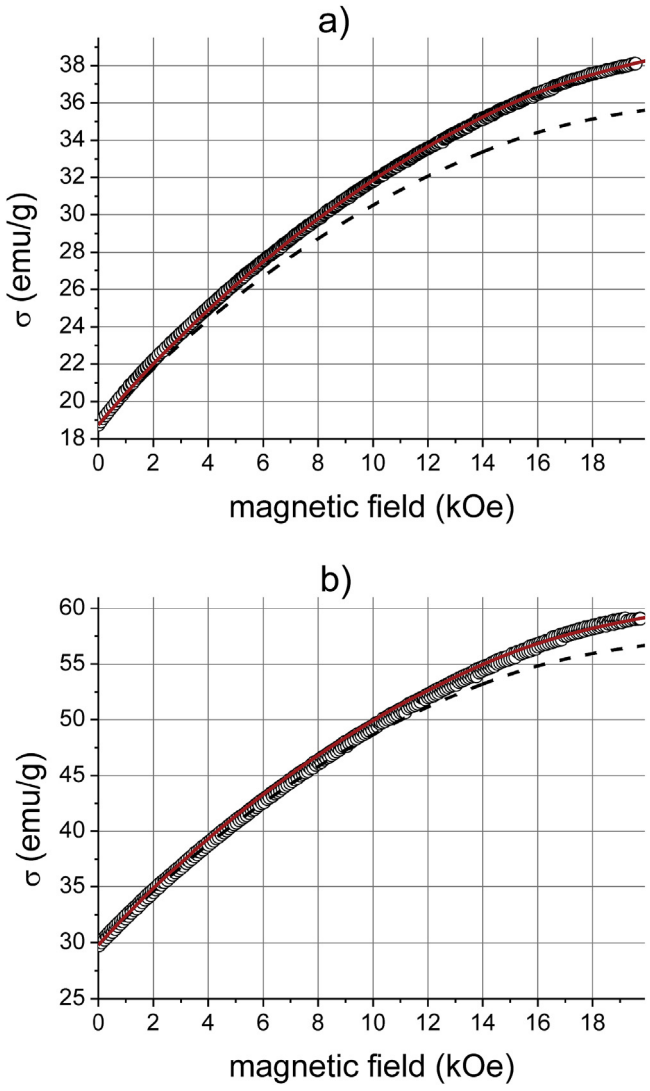

Fig. 7. Dependences σ (H) on the demagnetization sections of the hysteresis loops. The dots mean experiment, the lines – calculation. a) – Sample No 1, b) – sample No 4. The dotted lines are the numerical calculations. It describes the field dependence of contribution from rotation processes of magnetization vector $\sigma_{calc}(H)$ in $\sigma(H)$. The solid curves are the dependences of σ (H) taking into account the paraprocess.

Table 4
The basic characteristics of hysteresis loops.

temperature	80 K				295 K			
sample	No 1	No 2	No 3	No 4	No 1	No 2	No 3	No 4
σ_r, emu/g	27.7	43.9	41.3	44.7	18.7	28.5	28.1	29.8
$\sigma_{20\ kOe}$, emu/g	54.6	85.9	80.2	87.6	38.0	56.6	55.4	59.0
$\sigma_r/\sigma_{20\ kOe}$	0.51	0.51	0.52	0.51	0.49	0.5	0.51	0.5
H_c, kOe	4.43	4.87	4.57	4.96	4.96	5.49	5.27	5.63
σ_S, emu/g	–	–	–	–	37.5	57.2	56.2	59.5
$\chi_{para.}\cdot 10^3$, cm^3/g	–	–	–	–	0.133	0.115	0.125	0.125

in the book [1] it is noted, that the saturation magnetization of the bulk samples of Ba-M decreases with the increase of temperature faster than the anisotropy constant value k_1. It causes the growth of the anisotropy field H_{a1}. The coercive force H_c also increases.

The results of comparing the experimental magnetization curves at room temperature with the calculated ones are given in Fig. 7. The upper panel is for sample No 1 and the bottom panel is for sample No 4. The points in Fig. 7 are the sum of the demagnetization sections of the hysteresis loop from the first and third quadrants. The demagnetization sections of the hysteresis loops in negative magnetizing fields were inverted from the third to the first quadrant by replacing $-\sigma(H)$ by $\sigma(H)$ and $-H$ by H. The dashed curves in Fig. 7 show the dependences $\sigma_{calc}(H)$. They are calculated in accordance with the procedure described in Appendix A. The values of effective anisotropy fields H_{a1} used to calculate the magnetization curves are taken from the measurements of FMR line parameters (see Table 5).

The theoretical curves in Fig. 7 were designed using the following methodology. The calculated by the formula (A.6) magnetization curves normalized per unit $(M_H(H_0)/M_S)$ were multiplied by the specific saturation magnetization values σ_S. The values σ_S were chosen under the condition that the calculated curves by $H = 0$ coincide with the experimental specific saturation magnetization values σ_r. The values σ_S obtained due to this methodology are given in the 7th line of Table 4. It is evident from Table 4 that they are similar to the values $\sigma_{20\ kOe}$. According to Fig. 7, one can see a significant difference of the calculated $\sigma_{calc}(H)$ and the experimental curves with the increase of the magnetizing field. As

Table 5
Material parameters measured by means of FMR method.

Sample	No 1	No 2	No 3	No 4
M_S, Gs	198.0	302.0	296.7	314.2
$\gamma/2\pi$, GHz/kOe	2.80±0.02	2.80±0.02	2.80±0.02	2.80±0.02
H_{a1}, kOe	15.6±0.1	15.0±0.1	15.8±0.1	15.4±0.1
α, dim-less unit	0.07±0.01	0.07±0.01	0.10±0.01	0.07±0.01

mentioned above, the reason for this difference is a contribution from the paraprocess to the magnetization curve. The contribution from the paraprocess susceptibility (χ_{para}) on the dependence $\sigma(H)$ was calculated according to the following formula:

$$\sigma(H) = \sigma_{calc}(H) + \chi_{para}\, H. \quad (1)$$

The obtained values χ_{para} are given in the last line of Table 4. According to the table, χ_{para} of the sample No 1 with a wide particle size distribution is markedly larger than χ_{para} of the other samples. The dependences $\sigma(H)$ calculated according to formula (1) are shown in Fig. 7 with the solid lines. It can be seen that they practically coincide with the experimental data.

4.6. FMR spectra investigation

The FMR spectra investigation of powder and polycrystalline oxide ferrimagnetic with hexagonal crystalline structure gives an opportunity to determine a number of the magnetic parameters of these materials important for practical applications from the experiment. These are values and the sign of the magnetocrystalline anisotropy fields lengthwise the hexagonal axis (H_{a1}) and in the basal plane (H_Θ) as well as the values of the effective magnetomechanical ratio (γ) [25,37]. The procedure for determining these parameters using the FMR experiments for uniaxial powder hexaferrites with the easy magnetization axis is described in Appendix B.

The experimental FMR curves measured at the frequency of 53 GHz are shown with dots in Fig. 8. The imaginary parts of the diagonal component of the permeability tensor for the samples No 1 – No 4 calculated in the independent grains approach are shown with continuous lines. The experimental curves were normalized on the theoretical ones.

In the range of magnetizing fields (up to ~ 20 kOe) available for us only one maximum may be experimentally observed in the field close to $H_{||}$ (see the formula B.1 in Appendix B) which corresponds to the direction of easy magnetization. That is why only the values of anisotropy field H_{a1} and of effective magnetomechanical ratio $\gamma = \gamma_{||}$ were estimated based on experiment.

The saturation magnetization of a unit volume M_S that is necessary to calculate the components of the permeability tensor was determined in accordance with the formula $M_S = \sigma_S \cdot \rho$. Here, $\rho = 5.28$ g/cm^3 is the X-ray density of Ba-M hexaferrite [1]. The values of saturation magnetization, magnetomechanical ratios, anisotropy fields and damping constant α in the Landau–Lifshitz–Gilbert equation of motion of the magnetization vector for an individual monocrystalline grain are given in Table 5.

In accordance with the table the measured values of the magnetomechanical ratios for all samples coincide in the range of experiment error with the magnetomechanical ratio for the spin of a free electron. The same values of $\gamma/2\pi$ were obtained for Ba-M hexaferrite powders in the article [25]. The value of the effective anisotropy field of the samples demonstrates a weak dependence on the type of organic fuel. In addition, they are lower than the value $H_{a1} \approx 17$ kOe for bulk samples of hexaferrite Ba-M [1,5]. The possible reasons for this are the influence of the contributions from

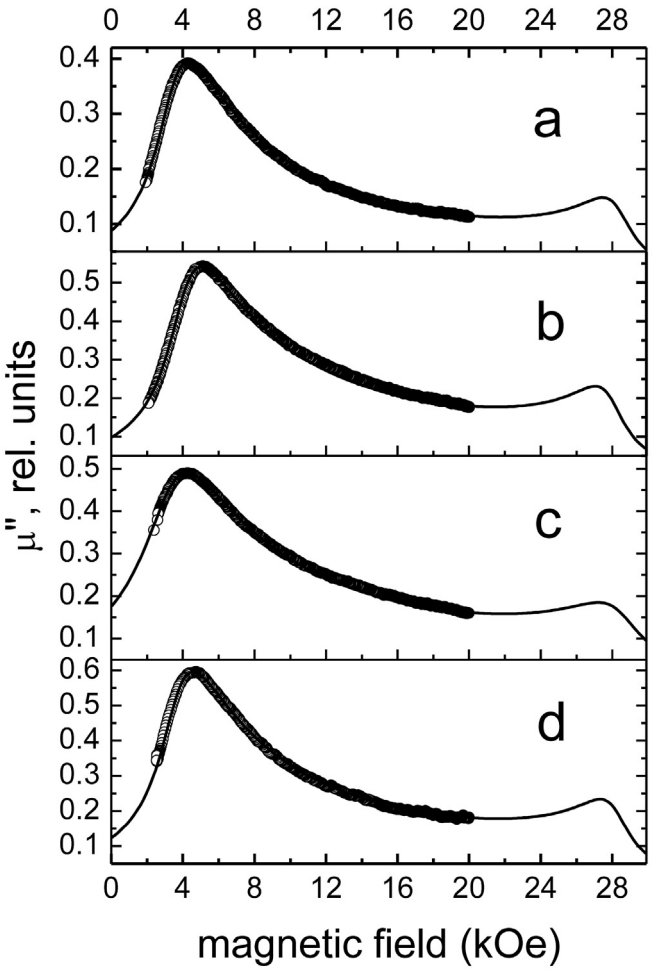

Fig. 8. Experimental (dots) and calculated (lines) FMR curves of the samples: sample No 1 (carbamide), b) – sample No 2 (sucrose), c) – sample No 3 (glycine) and d) – sample No 4 (citric acid). The measurement frequency is 53 GHz.

the anisotropy of the nanoparticles shape [25] and from the magnetic anisotropy of their defective surface layer [25,32,48]. The anisotropy of the defective surface layer of hexaferrite nanoparticles has the character of the easy magnetization plane. Therefore, the total anisotropy equal to the sum of the anisotropies of the unperturbed volume and the defective surface layer decreases.

According to Fig. 5 the samples Nos. 1, 3 have bigger particle sizes than the samples Nos. 2, 4. Therefore, large values of the anisotropy fields of these samples in comparison with the samples Nos. 2, 4 can be caused by a smaller contribution to the total anisotropy from the defective surface layer.

5. Conclusion

Thus, the studies of the organic fuel type effect on the phase composition, the structural characteristics and the magnetic properties of Ba-M hexaferrite nano-powders synthesized by sol-gel combustion have shown:

- The sample synthesized with the carbamide as an organic fuel has the least target phase $BaFe_{12}O_{19}$ output ~77%. Other samples contain more than 92% of Ba-M phase.

- The granulometric analysis revealed that the samples obtained with the use of carbamide (No 1) and glycine (No 3) demonstrate a wide particle size distribution and the average particles sizes are (120–135) nm. Whereas the samples synthesized with the use of sucrose (No 2) and citric acid (No 4) demonstrate narrower particle size distribution as well as smaller particle size: the sample No 2: (75–90) nm and the sample No 4: (90–105) nm.
- The samples No 2 and No 4 with the narrow particle size distribution have the biggest value of magnetization. At room temperature it is 56.6 and 59.0 emu/g respectively. The values obtained are similar to ones given in Refs. [5,17,25,26]. The paraprocess affects the magnetization processes significantly. The average paraprocess susceptibility for all samples is $\chi_{para.} \approx 0.125 \cdot 10^{-3}$ cm^3/g.
- The values of the magnetomechanical ratios estimated from the FMR experiments in the limits of the experimental error are the same as those for the spin moment of a free electron.
- The samples Nos. 1, 3 with bigger particle sizes than the samples Nos. 2, 4 have a large values of the anisotropy fields (15.6 kOe and 15.8 kOe respectively) in comparison with the samples Nos. 2, 4 (15.0 kOe and 15.4 kOe). The average value of the effective anisotropy field (15.5 kOe) is somewhat less than the value of H_{a1} for the polycrystalline samples synthesized with the conventional ceramics technology.

Acknowledgments

This work was performed under the Program for Improving Tomsk State University Competitiveness among the World's Leading Scientific and Educational Centers. Part of the work related to the synthesis of the materials was carried out within the framework of the state task of the FASO (Project No 0365-2018-0003) for the Tomsk Scientific Center, SB RAS. Part of the work related to the study of magnetization curves was partially funded by RFBR Grant No 16-02-00563.

Appendix A. Calculation of the magnetization curve for chaotically oriented ellipsoidal particles with uniaxial anisotropy. Non-interacting grains approach.

Let's assume, the sample consists of the chaotically oriented identical particles with uniaxial anisotropy of easy magnetization axis (EMA) type and the magnetic interaction among them can be neglected. Let's assume, the particles are ellipsoids of revolution and the axis of revolution coincides with the hexagonal axis *c*. The density of magnetic part of free energy (U) consists of contributions from the Zeeman energy (U_{Zee}), the energy demagnetizing fields of the particle (U_M) and the energy of magnetocrystalline anisotropy (U_{MKA}). In the spherical coordinate system with the axis z directed along the hexagonal axis c the density of the free energy $U = U_{Zee} + U_M + U_{MKA}$ can be written:

$$U = -M_S H_0[\sin(\Theta)\sin(\vartheta)\cos(\Phi-\varphi) + \cos(\Theta)\cos(\vartheta)] + \left[2\pi M_S^2\left(N_\perp - N_{||}\right) + k_1^{MKA}\right]\sin^2(\vartheta). \quad (A\ 1)$$

Here: M_S - saturation magnetization, H_0 – external magnetic field; $N_\perp, N_{||}$ - transverse and longitudinal demagnetizing factors of an ellipsoidal particle, where $2N_\perp + N_{||} = 1$; $k_1^{MKA} > 0$ – the first constant of the uniaxial magnetocrystalline anisotropy of EMA type; Θ, Φ – polar and azimuthal angles of the magnetizing field; ϑ, φ – polar and azimuthal angles of the magnetization vector.

The experimentally measured projection of the magnetization vector of the particle onto the direction of the magnetizing field is:

$$M_H(H_0,\Theta) = M_S\cos(\beta), \quad (A.2)$$

here β – the angle between the field $\vec{H}_0$ direction and the direction of the magnetization vector $\vec{M}(H_0,\Theta)$. In the spherical coordinate system defined above cos β is equal to:

$$cos(\beta) = \sin(\Theta)\sin(\vartheta)\cos(\Phi-\varphi) + \cos(\Theta)\cos(\vartheta). \quad (A.3)$$

The direction of the magnetization vector is determined by the two competing impacts: i) the external magnetic field that tend to turn the magnetization vector along the $\vec{H}_0$ direction and ii) the magnetocrystalline anisotropy, which deflects the magnetization vector to the EMA. The equilibrium angles ϑ_0, φ_0 of the magnetization vector are determined by the condition of the minimum of total energy (A.1):

$$\partial U/\partial\vartheta|_{\substack{\vartheta=\vartheta_0\\ \varphi=\varphi_0}} = 0,\ \partial U/\partial\varphi|_{\substack{\vartheta=\vartheta_0\\ \varphi=\varphi_0}} = 0. \quad (A.4)$$

As the task has cylindrical symmetry so the second equation of system (A.4) means that $\varphi_0 = \Phi$ and the vectors $\vec{M}(H_0,\Theta)$и $\vec{H}_0$ are located in one plane. In this case $cos(\beta) = \cos(\Theta - \vartheta_0)$. From the first equation (A.4) we have the transcendental equation to calculate the equilibrium angleϑ_0:

$$H_0\sin(\vartheta_0 - \Theta) + 0.5H_{a1}\sin(2\vartheta_0) = 0, \quad (A.5)$$

here $H_{a1} = 2k_1/M_S$, $k_1 = k_1^{MKA} + 2\pi M_S^2(N_\perp - N_{||})$ – is the constant of an effective anisotropy which includes the contributions from MCA and the anisotropy of particle form. After numerical computation of the dependence $\vartheta_0 = f(H_0,\Theta,H_{a1})$ the projection of magnetization vector of the separate grain on the direction of magnetic field $M_H(H_0,\Theta)$ is calculated. Then the summation on all chaotically oriented grains is carried out. The summation can be replaced with integration.

The easiest solution of this task is for demagnetization curves shown in Fig. 7. In this case the magnetization vectors of all grains as well as the magnetizing field are in the upper half plane and the angles Θ, ϑ_0 can vary in the range from 0 to $\pi/2$. The calculation of magnetization curve for a powder sample was performed in accordance with the formula:

$$M_H(H_0) = \int_0^{\pi/2} M_H(H_0,\Theta)\sin(\Theta)d\Theta. \quad (A.6)$$

The results of calculations in relative units ($M_H(H)/M_S$) are shown in Fig. A1 for several values of the anisotropy fields. When the magnetizing field is equal to zero all demagnetization curves take the value $M_H(0)/M_S = 0.5$ in accordance with the theory [47].

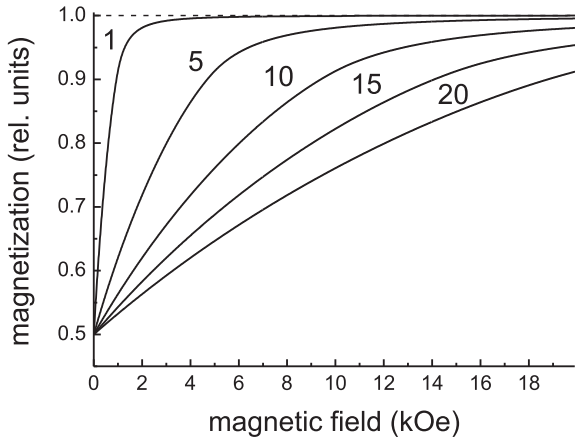

Fig. A1. The magnetization curves calculated for different values of the anisotropy fields. The digits in the curves denote the values of the anisotropy fields H_{a1} in kOe.

Appendix B. Determination the anisotropy fields values of uniaxial magnetic materials with EMA from FMR experiments on polycrystalline and powder samples

The polycrystalline and powder materials are macroscopically isotropic, but the presence of magnetic anisotropy in the individual grains manifests itself on their FMR curves of in the form of singularities – additional maxima and (or) steps. For powder materials with a large values of MCA fields the non-interacting grains approach is well executed since the anisotropy field $H_{a1} \gg 4\pi M_S$. The magnetic dipole interaction between the grains can be neglected in this case.

The foundations of FMR theory in the approximation of non-interacting grains were created by E. Schlömann for materials with cubic [49] and hexagonal [50] crystal structures. In the papers [51–53] this theory was generalized for materials with the anisotropic magnetomechanical ratio γ.

The start point non-interacting grains approach is the calculation of magnetic permeability of single monocrystalline single-domain grains of ellipsoidal shape when the magnetizing field has an arbitrary orientation relative to grains crystallographic axes. Further, by averaging over all possible orientations of $\vec{H}_0$, one can find the tensor of the magnetic permeability of the polycrystal.

The shortage of calculation methods in Refs. [49,50,53] is the impossibility to calculate the FMR resonance curve for uniaxial materials with EMA ($k_1^{MKA} > 0$) at the frequencies lower than the frequency of the natural ferromagnetic resonance (NFMR): $\omega_{E\Phi MP} = \gamma H_{a1}$. In the article [54] the method is proposed how to calculate the components of the permeability tensor (PT) for the uniaxial single-domain polycrystalline and powder samples at various frequencies. It is based on the solution of equation (A.5) for the given values of H_0 in the range of the angles Θ from 0 to $\pi/2$. Then the distribution of resonance frequencies $\omega_0[H_0,\vartheta_0(\Theta, H_0)]$ is calculated in accordance with the Smith-Suhl formula [55]. After that the values of PT components of a polycrystalline (powder) samples are calculated by the averaging the grain PT in the range of the angles Θ from 0 to $\pi/2$ for the given values H_0 and the frequency of microwave magnetic field ω.

In Refs. [49,50,53,54] it is shown that the FMR curves (or field dependences of imaginary components of the magnetic permeability tensor have two features: maxima and (or) steps. They are observed close to the values of magnetizing fields $H_{||}$ and $H_\perp$ that correspond with stationary directions on the angle dependence of the resonance field of a separate monocrystalline ellipsoidal grain. The values of resonance fields (frequencies) are calculated in accordance with formulas [54]:

$$\omega_{||} = \gamma_{||}\left[H_{||} + \left(\gamma_\perp/\gamma_{||}\right)H_{a1}\right],\ \omega_\perp = \gamma_\perp[H_\perp(H_\perp - H_{a1})]^{1/2},\ \omega_3 = \gamma_\perp\left(H_{a1}^2 - H_3^2\right)^{1/2}. \quad (B.1)$$

Here $\omega_{||}$ and $\omega_\perp$ are the resonance frequencies, $\gamma_{||}$ and $\gamma_\perp$ are the magnetomechanical ratios for the directions along the hexagonal axis c ($\Theta = 0$) and in the basal plane ($\Theta = \pi/2$) respectively. If the magnetomechanical ratio is isotopic then $\gamma_{||} = \gamma_\perp = \gamma$. The resonance at the frequency ω_3 is observed at the frequencies lower than ω_{NFMR}. There is no resonance at the frequency $\omega_{||}$ in this case. In further calculations it was assumed that in comparison with k_1^{MKA} the high-order MCA constants can be neglected. The value of the anisotropy field in the basal plane is equal to the anisotropy field along the hexagonal axis $H_\Theta = H_{a1}$ in this case [53,54].

The results of the comparison of field dependences of maxima and (or) steps on the resonance curves of a polycrystalline sample calculated for different frequencies with the calculation of the field dependences of the FMR resonance frequencies of the single-crystal grains using formulas (B.1) are shown in Fig. B1. The solid lines in Fig. B1 are the calculations by formulas (B.1). The calculations are made for the following values: $H_{a1} = 10$ kOe, $\gamma = 2.8$ GHz/kOe. The damping constant in the Landau–Lifshitz–Gilbert equation of motion of the magnetization vector for the monocrystalline grain is $\alpha = 0.1$. The fields of maximums on the FMR curves of polycrystalline sample are marked with (H_M). The fields of maximums on the derivatives of these curves are marked with (H_{MD}). It is seen that the fields of maximums H_{MD} of the derivatives (the inflection points on the FMR curves) at the corresponding frequencies are closer to the dependencies calculated in accordance with the formulas (B.1) than the fields of maximum on the resonance curves H_M.

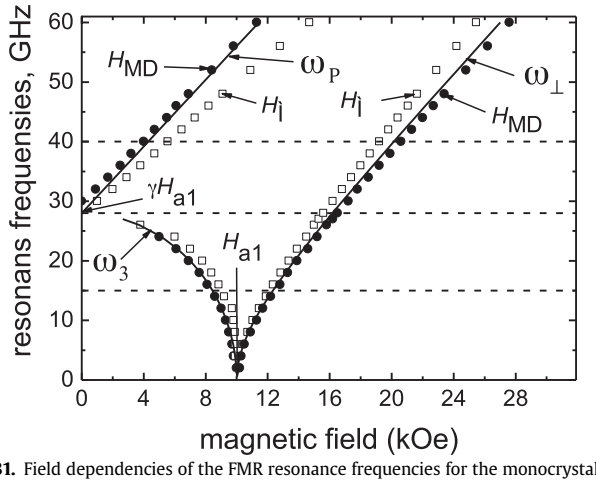

Fig. B1. Field dependencies of the FMR resonance frequencies for the monocrystalline grain (continuous lines, calculation according to formulas (B.1)). Blank squares are the fields of maximums on the resonance curves of polycrystals (H_M). Shaded dots are the fields of maximums on their derivatives (MD). The dashed lines indicate the frequencies of microwave radiation, for which calculation of the resonance curves of the polycrystalline samples are below (Fig. B2).

The FMR curves of polycrystalline samples for $H_{a1} = 10$ kOe, $\gamma = 2.8$ GHz/kOe are shown in Fig. B2. They are calculated for the frequencies (in GHz) that are marked with numbers at the resonance curves. The vertical sections on the FMR curves are the values of resonance magnetic fields $H_{||}$, $H_\perp$, H_3 calculated by the formulas (B.1). The intensity of resonance peak at the frequency of 10^{-3} GHz is reduced by 100 times. In fact, it is a delta-shaped jump in the imaginary part of the magnetic permeability at the magnetization

reversal point. The magnetization vector is reoriented from EMA to the hard magnetization plane at the value of magnetic field $H_0 = H_{a1}$. The similar effect was observed while investigating the FMR in the thin magnetic films in the paper [56].

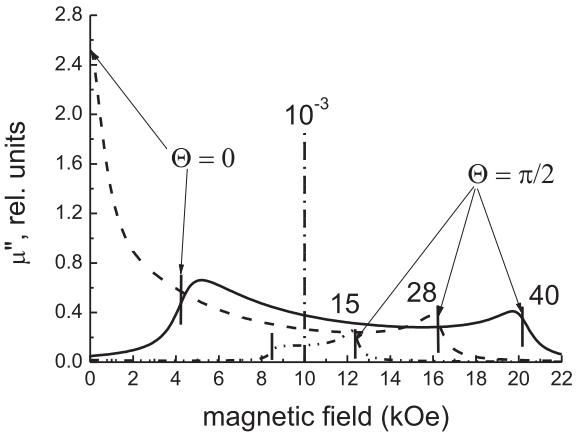

Fig. B2. Resonance curves of polycrystalline samples calculated for the following parameters: $H_{a1} = 10$ kOe, $M_S = 0.3$ kGs, damping constant $\alpha = 0.05$. The numbers at the curves are the values of the frequency in GHz. The vertical sections on the FMR curves are the values of resonance magnetic fields $H_{||}$, $H_{\perp}$, H_3 calculated by the formulas (B.1).

Thus, the FMR spectra investigation aimed at establishing the values of anisotropy fields is to be better conducted at the frequencies higher than the NFMR frequency $\omega > \gamma H_{a1}$. In this case the imaginary part of magnetic permeability is significantly bigger than in the case $\omega < \gamma H_{a1}$. If the experimental FMR curves have two maxima (or steps) on the resonance curve one can calculate both the anisotropy of magneto-mechanical ratio $(\gamma_{||}, \gamma_{\perp})$ and the values of magnetocrystalline anisotropy fields H_{a1} and H_{Θ} [37].

Thereby the processing of experimental FMR spectra for polycrystalline and powder samples with EMA was conducted according to the following method:

1. The FMR curves are measured in a given frequency range, which depends on the magnitude of the anisotropy field.
2. The frequency dependences of the magnetizing fields corresponding to the maxima of the derivatives on the resonance curves are constructed. The values of magneto-mechanical ratios $\gamma_{||}, \gamma_{\perp}$ and the values of anisotropy field's H_{a1}, H_{Θ} are established due to the processing of these dependences by means of the least-square technique in accordance with the formulas (B.1).
3. The values of magnetomechanical ratios and the anisotropy fields are made more precise by means of detailed comparison of the forms of calculated and experimental FMR curves.

References

[1] J. Smit, H.P.J. Wijn, Ferrite. Physical Properties of Ferrimagnetic Oxides in Relation to Their Technical Applications, Philips' Technical Library, Eindhoven, 1959.
[2] B. Wartenberg, Messung der elektromagnetischen Stoffkonstanten μ und ε von Ferriten im mm-Wellengebiet, Z. Angew. Phys. 24 (1968) 211–217.
[3] H. Severin, J.P. Stoll, Permeabilität einiger Ferrite mit magnetischen Verlusten im Bereich der Zentimeter- und Millimeterwellen, Z. Angew. Phys. 23 (1967) 209–212.
[4] H.S. Cho, S.S. Kim, M-Hexaferrites with planar magnetic anisotropy and their application to high-frequency microwave absorbers, IEEE Trans. Magn. 35 (1999) 3151–3153.
[5] R.C. Pullar, Hexagonal ferrites: a review of the synthesis, properties and applications of hexaferrite ceramics, Prog. Mater. Sci. 57 (2012) 1191–1334.
[6] L.I. Rabkin, S.A. Soskin, B. Sh Epshtein, Ferrites, Energiya, Leningrad, 1968 ([in Russian]).
[7] Yu Sitidze, H. Sato, Ferrites, Mir, Moscow, 1964 ([in Russian]).
[8] A.V. Komarov, M.D. Nersesyan, P.B. Avakyan, A.G. Merzhanov, Self-propagating high-temperature synthesis of ferrites, Int. J. Self-Propag. High-Temp. Synth. 2 (1993) 239–246.
[9] A.V. Komarov, P.B. Avakyan, M.D. Nersesyan, Self-propagating high-temperature synthesis of strontium hexaferrites, Combust. Explos. Shock Waves 29 (1993) 597–602.
[10] P.B. Avakyan, K.S. Martirosyan, S.O. Mkrtchyan, Phase formation during SHS of barium ferrite, Int. J. Self-Propag. High-Temp. Synth. 1 (1992) 551–554.
[11] V.I. Itin, A.I. Kirdyashkin, R.V. Minin, E.P. Naiden, R.M. Gabbasov, Yu M. Maksimov, Self-propagating high-temperature synthesis of hexagonal ferrimagnetic oxide with a W-type structure, Izv. Vyssh. Uchebn. Zaved., Tsvet. Metall. 5 (2006) 83–88.
[12] E.P. Naiden, V.A. Zhuravlev, R.V. Minin, V.I. Suslyaev, V.I. Itin, E. Yu Korovin, Structural and magnetic properties of SHS-produced multiphase W-type hexaferrites: influence of radiation-thermal treatment, Int. J. Self-Propag. High-Temp. Synth. 24 (2015) 148–151.
[13] E.P. Naiden, V.A. Zhuravlev, R.V. Minin, V.I. Itin, Influence of radiation–thermal treatment on phase composition and structural parameters of the SHS product based on W-type hexaferrite, Russ. Phys. J. 56 (2013) 674–680.
[14] R.V. Minin, V.I. Itin, E.P. Naiden, V.A. Zhuravlev, Mechanisms of the self-propagating high-temperature synthesis, phase composition, and magnetic properties of complex oxide ferrimagnets with M-structure, Russ. J. Non-Ferrous Metals 53 (2012) 410–414.
[15] M.V. Kuznetsov, Q.A. Pankhurst, I.P. Parkin, Novel SHS routes to CoTi-doped M-type ferrites, J. Mater. Sci. Mater. Electron. 12 (2001) 533–536.
[16] S. Castro, M. Gayoso, J. Rivas, J.M. Greneche, J. Mira, C. Rodriguez, Structural and magnetic properties of barium hexaferrite nanostructured particles prepared by the combustion method, J. Magn. Magn. Mater. 152 (1996) 61–69.
[17] J. Huang, H. Zhang, W. Li, Synthesis and characterization of nano-crystalline $BaFe_{12}O_{19}$ powders by low temperature combustion, Mater. Res. Bull. 38 (2003) 149–159.
[18] L. Junliang, Z. Yanwei, G. Cuijing, Z. Wei, Y. Xiaowei, One-step synthesis of barium hexaferrite nano-powders via microwave-assisted sol-gel auto-combustion, J. Eur. Ceram. Soc. 30 (2010) 993–997.
[19] A. Mali, A. Ataie, Influence of the metal nitrates to citric acid molar ratio on the combustion process and phase constitution of barium hexaferrite particles prepared by sol-gel combustion method, Ceram. Int. 30 (2004) 1979–1983.
[20] A. Mali, A. Ataie, Influence of Fe/Ba molar ratio on the characteristics of Ba-hexaferrite particles prepared by sol-gel combustion method, J. Alloys Compd. 399 (2005) 245–250.
[21] A. Mali, A. Ataie, Structural characterization of nano-crystalline $BaFe_{12}O_{19}$ powders synthesized by sol-gel combustion route, Scripta Mater. 53 (2005) 1065–1070.
[22] D. Bahadur, S. Rajakumar, A. Kumar, Influence of fuel ratios on auto combustion synthesis of barium ferrite nano particles, J. Chem. Sci. 118 (2006) 15–21.
[23] G. Xu, H. Ma, M. Zhong, J. Zhou, Y. Yue, Z. He, Influence of pH on characteristics of $BaFe_{12}O_{19}$ powder prepared by sol-gel auto-combustion, J.M.M.M 301 (2006) 383–388.
[24] L. Junliang, Z. Wei, G. Cuijing, Z. Yanwei, Synthesis and magnetic properties of quasi-single domain M-type barium hexaferrite powders via sol-gel auto-combustion: effects of pH and the ratio of citric acid to metal ions (CA:M), J. Alloys Compd. 479 (2009) 863–869.
[25] E.P. Naiden, V.A. Zhuravlev, R.V. Minin, V.I. Itin, E.Yu Korovin, Static and dynamic magnetic properties of nanosized barium hexaferrite powders prepared by the Sol-Gel combustion method, Russ. Phys. J. 58 (2015) 125–132.
[26] F. Ebrahimi, S.S. Yazdi, Ferromagnetic resonance investigation of hexaferrite nanoparticles prepared by sol-gel auto-combustion method, J. Supercond. Nov. Magn. (2016), https://doi.org/10.1007/s10948-016-3881-8.
[27] S. Abedini Khorrami, R. Islampour, H. Bakhtiari, Q. Sadr Manuchehri Naeini, The effect of molar ratio on structural and magnetic properties of $BaFe_{12}O_{19}$ nanoparticles prepared by sol-gel autocombustion method, Int. J. Nano Dimens. (IJND) 3 (2013) 191–197.
[28] N. Rezlescu, E. Rezlescu, C. Doroftei, P.D. Popa, Li and Ba ferrite nanoparticles prepared by selfcombustion, Phys. Status Solidi (C) 1 (2004) 3640–3643.
[29] H. Shang, J. Wang, Q. Liu, Synthesis and characterization of nanocrystalline $BaFe_{12}O_{19}$ obtained by using glucose as a fuel, Mater. Sci. Eng., A 456 (2007) 130–132.
[30] Y.Y. Meng, M.H. He, Q. Zeng, D.I. Jiao, S. Shukla, R.V. Ramanujan, Z.W. Liu, Synthesis of barium ferrite ultrafine powder by a sol-gel combustion method using glycine gels, J. Alloys Compd. 583 (2014) 220–225.
[31] R. Grossinger, A critical examination of the law of approach to saturation. I. Fit procedure, Phys. Status Solidi (A) 66 (1981) 665–674.
[32] Z.V. Golubenko, L.P. Ol'khovik, Yu A. Popkov, Z.I. Sizova, A.S. Kamzin, Magnetic anisotropy of a system of nanocrystalline BaO-$6Fe_20_3$ particles, Phys. Solid State 40 (1998) 1718–1720.
[33] R. Grossinger, Correlation between the inhomogeneity and the magnetic anisotropy in polycrystalline ferromagnetic materials, J. Magn. Magn. Mater. 28 (1982) 137–142.
[34] G. Asti, S. Rinaldi, Singular points in the magnetization curve of a polycrystalline ferromagnet, J. Appl. Phys. 45 (1974) 3600–3610.
[35] R. Grossinger, Generation, measuring technique and application of pulsed fields, J. Alloys Compd. 369 (2004) 5–9.
[36] S.K. Misra, M.V. Rane, C. Srivastava, D. Bahadur, A variable temperature

ferromagnetic resonance study of Ni-Zr-substituted non-stoichiometric barium ferrite samples, J. Magn. Magn. Mater. 187 (1998) 93–104.
[37] E.P. Naiden, V.A. Zhuravlev, V.I. Itin, R.V. Minin, V.I. Suslyaev, O.A. Dotsenko, Structure and static and dynamic magnetic properties of $Sr(Co_xTi_x)Fe_{12-2x}O_{19}$ hexaferrites produced by self-propagating high-temperature synthesis, Russ. Phys. J. 55 (2013) 869–877.
[38] S.K. Chawla, P. Kaur, R.K. Mudsainiyan, S.S. Meena, S.M. Yusuf, Effect of fuel on the synthesis, structural, and magnetic properties of M-type hexagonal $SrFe_{12}O_{19}$ nanoparticles, J. Supercond. Nov. Magn. 28 (2015) 1589–1599.
[39] P. Kaur, S.K. Chawla, S.B. Narang, K. Pubby, Structural, magnetic and microwave absorption behavior of Co-Zr substituted strontium hexaferrites prepared using tartaric acid fuel for electromagnetic interference suppression, J. Magn. Magn. Mater. 422 (2017) 304–314.
[40] D.A. Velikanov, Vibration magnetic meter, Ru Patent No 2341810 (2008).
[41] J. Kreisel, G. Lucazeau, H. Vincent, Raman spectra and vibrational analysis of $BaFe_{12}O_{19}$ hexagonal ferrite, J. Solid State Chem. 137 (1998) 127–137.
[42] J. Kreisel, S. Pignard, H. Vincent, J.P. Senateur, G. Lucazeau, Raman study of $BaFe_{12}O_{19}$ thin films, Appl. Phys. Lett. 73 (1998) 1194–1196.
[43] F.M. Silva Jr., C.W.A. Paschoal, Spin-phonon coupling in $BaFe_{12}O_{19}$ M-type hexaferrite, J. Appl. Phys. 116 (2015), 244110.
[44] J.F. Lu, C.J. Tsai, Hydrothermal phase transformation of hematite to magnetite, Nanoscale Res. Lett. 9 (2014) 230.
[45] X. Zhang, Y. Niu, X. Meng, Y. Li, J. Zhao, Structural evolution and characteristics of the phase transformations between α-Fe_2O_3, Fe_3O_4 and γ-Fe_2O_3 nanoparticles under reducing and oxidizing atmospheres, J. Cryst. Eng. Commun. 40 (2013) 8166–8172.
[46] F.J. Morin, Magnetic susceptibility of αFe_2O_3 and αFe_2O_3 with added titanium, Phys. Rev. 78 (1950) 819–820.
[47] E.C. Stoner, E.P. Wohlfart, A mechanism of magnetic hysteresis in heterogeneous alloys, IEEE Trans. Magn. 27 (1991) 3475–3518.
[48] S.P. Gubin, Y.A. Koksharov, G.B. Khomutov, G.Y. Yurkov, Magnetic nanoparticles: preparation, structure and properties, Russ. Chem. Rev. 74 (2005) 489–520.
[49] E. Schlömann, Ferromagnetic resonance in polycrystalline ferrites with large anisotropy – I: general theory and application to cubic materials with a negative anisotropy constant, J. Phys. Chem. Solid. 6 (1958) 257–266.
[50] E. Schlömann, R.V. Jones, Ferromagnetic resonance in polycrystalline ferrites with hexagonal crystal structure, J. Appl. Phys. 30 (1959) S177–S178.
[51] К.В. Vlasov, В.Н. Ishmuhametov, The equation of motion for the magnetization in magnetic media, Fiz. Metal. i Metalloved 11 (1961) 3–9.
[52] A.G. Gurevich, V.A. Sanina, E.I. Golovenchits, S.S. Starobinets, Resonance in magnetically ordered crystals with anisotropic g factors, J. Appl. Phys. 40 (1969) 1512–1517.
[53] V.A. Zhuravlev, Ferromagnetic resonance in the polycrystalline Hexagonal ferrites $Co_{2-x}Zn_xW$, Phys. Solid State 41 (1999) 956–959.
[54] V.A. Zhuravlev, V.A. Meshcheryakov, Magnetic susceptibility tensor of anisotropic ferromagnetic magnetized media, Russ. Phys. J. 56 (2014) 1387–1397.
[55] A.G. Gurevich, G.A. Melkov, Magnetization Oscillations and Waves, CRC Press., 1996.
[56] B.A. Belyaev, A.V. Izotov, S. Ya Kiparisov, Singularity in high-frequency susceptibility of thin magnetic films with uniaxial anisotropy, JETP Lett. 74 (2001) 226–230.